*metals*

MDPI

*Article*

# Cost-Effective Manufacturing of Ti-6Al-4V Filler Wire from As-Cast Ingot via Processing Map-Guided Design for Wire Arc Additive Manufacturing

**Anoop Kumar Maurya [1,2], Jong-Taek Yeom [1,*], Jae H. Kim [1], Junha Yang [1,*], Chan Hee Park [1], Jae-Keun Hong [1] and Nagireddy Gari Subba Reddy [2]**

[1] Lightweight Materials Research Division, Korea Institute of Materials Science, Changwon 51508, Republic of Korea
[2] School of Materials Science and Engineering, Engineering Research Institute, Gyeongsang National University, Jinju 52828, Republic of Korea
* Correspondence: yjt96@kims.re.kr (J.-T.Y.); jhyang@kims.re.kr (J.Y.)

**Abstract**

Wire and arc additive manufacturing (WAAM) is a cost-efficient technology for large-scale production; however, the high cost of Ti-6Al-4V filler wire, primarily associated with conventional billet-based thermomechanical processing, remains a critical limitation. This study proposes a direct and cost-effective manufacturing route for Ti-6Al-4V filler wire from an as-cast ingot, enabled by processing map-guided thermomechanical design. Hot deformation behavior was systematically investigated for the as-cast ingot, the β-forged billet, and the α + β-forged billet over 700–1200 °C and strain rates of 0.01–10 $s^{-1}$. An artificial neural network (ANN)-assisted correction was employed to compensate for adiabatic heating, enabling reliable construction of processing maps and identification of stable deformation domains associated with dynamic recrystallization (DRX). The optimized deformation conditions derived from the processing maps were directly applied to hot-rolling, followed by room-temperature wire drawing. As a result, high-quality Ti-6Al-4V filler wire with a diameter of 1.7 mm was successfully fabricated. Microstructural analysis revealed deformation-induced refinement and alignment of the α phase, with variations depending on the initial state. Despite relatively coarser features, the wire fabricated from the as-cast ingot exhibited a tensile strength of 1408 MPa and elongation of 6.7%, demonstrating tensile properties comparable to those of the wires fabricated from the forged billets. These results provide direct experimental validation that processing map-guided design enables the direct conversion of as-cast Ti-6Al-4V ingots into high-quality filler wire. The proposed approach offers a simplified and economically competitive alternative to conventional billet-based processing routes for WAAM applications.

**Keywords:** Ti-6Al-4V; wire arc additive manufacturing (WAAM); processing map-guided design; as-cast ingot; cost-effective manufacturing; filler wire

Check for updates

Academic Editor: Guido Di Bella

Received: 25 July 2026
Revised: 16 August 2026
Accepted: 19 August 2026
Published: 29 August 2026

**Copyright:** © 2026 by the authors. Licensee MDPI, Basel, Switzerland. This article is an open access article distributed under the terms and conditions of the Creative Commons Attribution (CC BY) license.

## 1. Introduction

Titanium and its alloys are widely used in aerospace and energy sectors due to their high specific strength and excellent corrosion resistance [1–4]. However, the fabrication of high-performance Ti-6Al-4V components remains costly and challenging, particularly when complex geometries are required. Conventional manufacturing typically involves

extensive subtractive machining of forged billets to achieve near-net-shape components, resulting in significant material waste and high processing costs [5].

Additive manufacturing (AM) has emerged as a promising alternative for producing near-net-shape Ti-6Al-4V components with reduced material waste and tooling requirements. Among various AM techniques, such as selective laser melting (SLM), electron beam melting (EBM), and laser engineered net shaping (LENS), limitations remain in terms of part size, deposition rate, and productivity [6]. In contrast, wire and arc additive manufacturing (WAAM) offers high deposition rates, scalability to meter-sized components, and improved material utilization at a relatively low cost [5,7]. These advantages make WAAM particularly attractive for large-scale Ti-6Al-4V component manufacturing. In WAAM, the filler wire serves as the primary feedstock, and its production cost significantly influences the overall manufacturing cost.

Previous studies on Ti-6Al-4V filler-wire production have primarily focused on thermomechanical processing and wire-drawing behavior rather than direct conversion of as-cast ingots into WAAM feedstock. Conventional Ti-6Al-4V wire manufacturing generally involves multiple thermomechanical processing steps, in which as-cast material is subjected to β forging and subsequent α + β forging to break down the coarse cast microstructure, followed by hot rolling and multi-pass wire drawing to obtain the required wire diameter [8–10]. Hu et al. [8], for example, investigated the effects of multi-pass drawing strain and subsequent heat treatment on the microstructure, texture, and mechanical properties of Ti-6Al-4V wire. Other studies have investigated alternative drawing strategies, including hot drawing and dieless drawing, to improve the formability and processing efficiency of Ti-6Al-4V wire. Naughton and Tiernan [9] investigated dieless drawing of ELI Ti-6Al-4V and demonstrated the influence of drawing parameters on achievable cross-sectional reduction. More recently, hot-drawing studies have examined the effects of drawing temperature, drawing speed, and deformation on the deformation behavior and microstructural evolution of Ti-6Al-4V wire. These studies demonstrate that the thermomechanical processing conditions strongly influence the final microstructure, texture, ductility, and strength of Ti-6Al-4V wire.

However, most existing approaches begin with wrought or pre-processed Ti-6Al-4V feedstock and therefore retain the conventional requirement for intermediate thermomechanical processing of the cast material. In particular, limited attention has been given to directly converting an as-cast Ti-6Al-4V ingot into filler wire while simultaneously controlling deformation stability and microstructural refinement. Furthermore, systematic integration of processing-map analysis with experimental wire fabrication has not been sufficiently explored for this purpose. Therefore, a processing-map-guided approach that can identify stable deformation conditions and enable direct processing of as-cast Ti-6Al-4V into WAAM filler wire represents an important research opportunity.

Processing maps are widely used to identify optimal deformation conditions by correlating deformation parameters with microstructural evolution and deformation mechanisms [11]. The hot deformation behavior of Ti-6Al-4V is highly sensitive to temperature, strain rate, and strain and involves complex interactions between work hardening and dynamic softening mechanisms such as dynamic recovery (DRV) and dynamic recrystallization (DRX) [12–16]. In particular, DRX plays a critical role in improving deformation stability and refining the microstructure during high-temperature processing. However, the accurate construction of processing maps requires reliable isothermal flow stress data. In practice, hot deformation experiments often exhibit non-isothermal behavior due to adiabatic heating, leading to deviations in flow stress measurements. To overcome this limitation, artificial neural network (ANN)-based approaches have been employed to model the complex nonlinear relationships between deformation parameters and flow

stress [17,18]. Nevertheless, previous studies have primarily focused on individual initial microstructures, and a comprehensive comparison of Ti-6Al-4V in the as-cast, β-forged, and β → α + β-forged states in the context of process design remains limited. Furthermore, the application of ANN-assisted correction for non-isothermal flow behavior in constructing processing maps for direct process design has not been sufficiently explored.

The industrial relevance of the proposed approach lies in its potential for the high-volume production of titanium filler wire required for large-scale wire-based additive manufacturing. A stable supply of filler wire with consistent chemical composition, dimensional accuracy, surface quality, and mechanical properties is essential for reliable WAAM deposition. Since large titanium components may require substantial quantities of filler wire, increasing wire-production capacity can facilitate continuous and scalable WAAM. Moreover, the development of an efficient filler-wire manufacturing route has the potential to reduce material and processing costs, improve supply-chain reliability, and reduce dependence on imported titanium filler wire.

In this study, a processing map-guided thermomechanical design approach is proposed to enable direct fabrication of Ti-6Al-4V filler wire from an as-cast ingot. Hot deformation behavior was systematically investigated using specimens with three different initial states, namely the as-cast ingot, the single-stage β-forged billet, and the two-stage β → α + β-forged billet. The economic advantage of the proposed route originates primarily from the elimination of intermediate β- and α + β-forging operations, which reduces the number of thermomechanical processing stages, reheating cycles, material handling operations, and associated energy and tooling requirements. ANN-assisted correction was applied to obtain reliable flow stress data for processing map construction. The deformation characteristics and microstructural evolution were comparatively analyzed to identify optimal processing domains for direct processing from the as-cast ingot. Based on the optimized conditions, hot-rolling and subsequent wire drawing were performed to fabricate high-quality Ti-6Al-4V filler wire. This work aims to establish a simplified and cost-effective processing route by linking deformation behavior, microstructural evolution, and practical wire fabrication.

## 2. Materials and Methods

The Ti-6Al-4V used in this study was produced via a vacuum arc remelting (VAR) process (HVM Co., Ltd., Anyang, Republic of Korea) using Ti-6Al-4V scrap. The chemical composition of the as-cast Ti-6Al-4V ingot used in this study is summarized in Table 1. The as-cast ingot was subsequently processed into two types of billets: a β-forged billet produced by single-stage forging in the β-phase region (1140 °C) and a β → α + β-forged billet produced by two-stage forging consisting of primary forging in the β-phase region (1140 °C) followed by secondary forging in the α + β-phase region (920 °C). For convenience, the β → α + β-forged billet is hereafter referred to as the α + β-forged billet. The representative β-transus temperature ($T_\beta$) of the Ti-6Al-4V was determined to be approximately 990 °C based on microstructural observations after heat treatment and water quenching.

**Table 1.** Chemical composition of the as-cast Ti-6Al-4V ingot used in this study (wt.%).

| Ti | Al | V | Fe | C | O | N | H |
|---|---|---|---|---|---|---|---|
| Bal. | 6.09 | 4.02 | 0.25 | 0.04 | 0.17 | 0.02 | 0.003 |

Cylindrical specimens with a diameter of 8 mm and a height of 12 mm were machined from each condition for hot deformation testing. Hot compression tests were conducted using a Gleeble 3800 thermo-mechanical simulator (Dynamic Systems Inc., Poestenkill,

NY, USA) over a temperature range of 700–1200 °C and strain rates of 0.01–10 $s^{-1}$ up to a 50% reduction in height. Prior to deformation, the specimens were heated to the target temperature at a rate of 10 °C/s and held for 5 min to ensure thermal homogeneity. The flow stress and instantaneous temperature were continuously recorded during deformation, and the specimens were then water-quenched to preserve the deformed microstructure.

For microstructural characterization, the deformed specimens were sectioned parallel to the compression axis. Optical microscopy was performed after standard mechanical polishing and etching using Kroll's reagent (2% hydrofluoric acid + 2% nitric acid + 96% DI water). Electron backscatter diffraction (EBSD) analysis was conducted on electropolished specimens (95% methanol + 5% perchloric acid, −30 °C, 20 V) using a field-emission scanning electron microscope (FESEM, JEOL JSM-7001F) (Tokyo, Japan). The EBSD analysis focused on the plastically deformed regions to correlate deformation behavior with microstructural evolution. Processing maps were constructed based on the corrected flow stress data to identify stable deformation domains for each initial microstructure. The optimized deformation conditions obtained from the processing maps were subsequently applied to hot-rolling of the as-cast ingot, followed by room-temperature wire drawing to fabricate Ti-6Al-4V filler wire with a final diameter of 1.7 mm for WAAM applications.

Tensile tests were performed using three filler wire specimens for each condition with a diameter of 1.6 mm and a length of 50 mm. The tests were conducted at ambient temperature at an initial strain rate of $1 \times 10^{-3}$ $s^{-1}$ using a universal testing machine (EZ Test, Shimadzu, Kyoto, Japan) equipped with a 5 kN load cell. To ensure the reliability and reproducibility of the data, at least three independent tests were performed under identical conditions.

## 3. ANN Model Development

An artificial neural network (ANN) model was developed to correct the non-isothermal flow stress ($\sigma_{non\text{-}iso}$) obtained during hot deformation and to estimate the corresponding isothermal flow stress ($\sigma_{iso}$) required for reliable processing map construction. The ANN model enables modeling of complex nonlinear relationships among deformation parameters without requiring explicit constitutive equations. The model architecture consisted of three input neurons representing temperature, strain rate, and strain and one output neuron corresponding to the corrected flow stress. A backpropagation algorithm with a sigmoid activation function was employed for ANN model training [19,20]. A total of 645 datasets obtained from the hot deformation experiments were used to develop independent ANN models for the as-cast ingot, β-forged billet, and α + β-forged billet conditions. Each ANN model was trained and tested exclusively using the datasets corresponding to its respective material condition. For each model, 550 datasets were allocated for training and 95 datasets were independently selected for testing. The testing datasets were not used during the training process to ensure an independent evaluation of the predictive performance of the developed models. The ANN hyperparameters, including the number of hidden neurons, learning rate, momentum coefficient, and number of iterations, were optimized by minimizing the root mean square error (RMSE) and prediction error (Etr). The optimized ANN architecture and training parameters were then used to establish the final prediction models. Further details regarding the ANN training procedure and optimization methodology are provided in previous studies [21,22]. The performance of the developed models was evaluated using both training and testing datasets. As shown in Figure 1, the correlation coefficients (Pearson's r) and adjusted $R^2$ values were close to unity for all conditions, indicating high prediction accuracy. These results confirm that the ANN

model effectively corrects flow stress data over a wide range of deformation conditions, thereby enabling reliable processing map construction for process design.

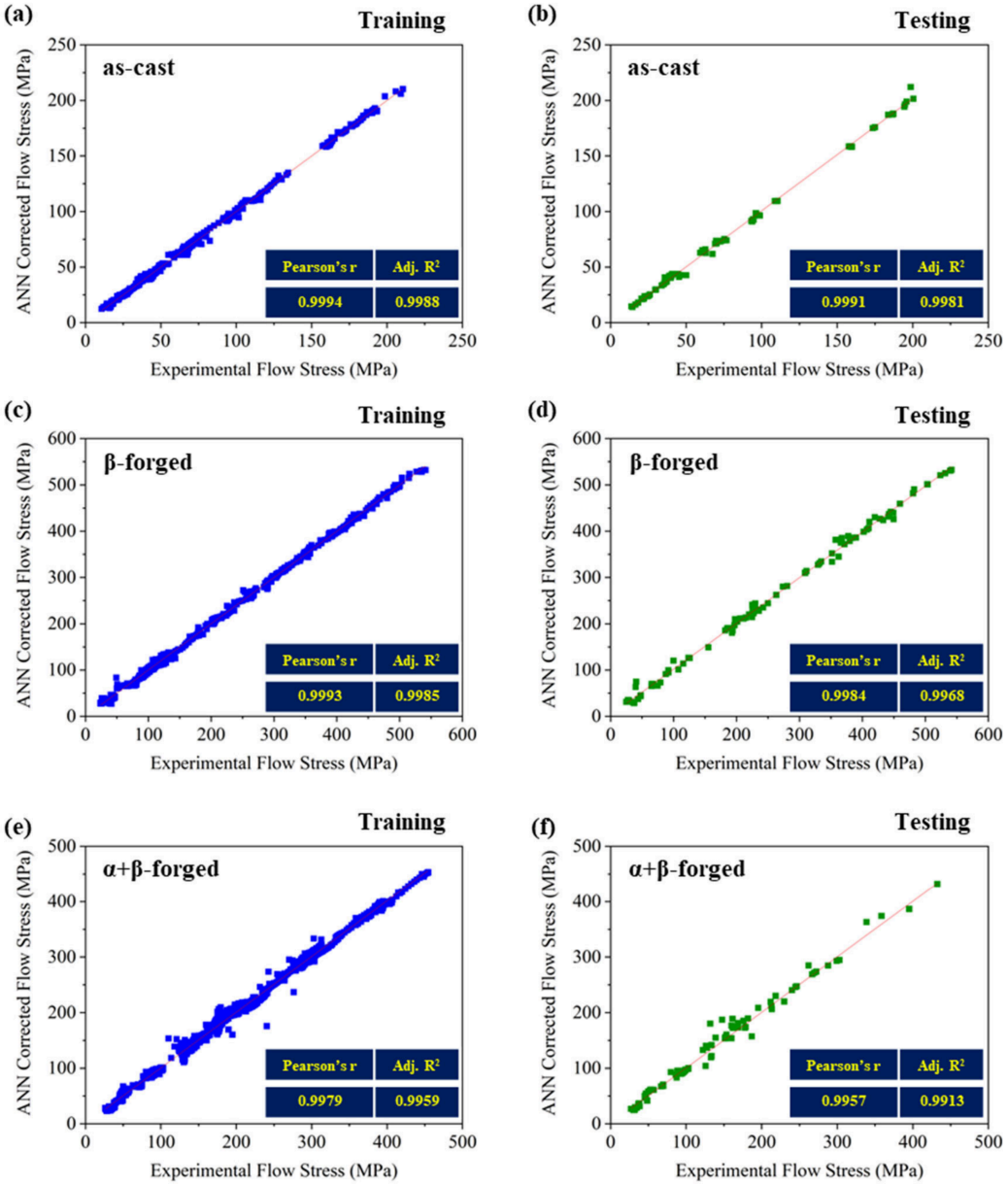



**Figure 1.** Comparison of ANN-corrected and experimental flow stress data for Ti-6Al-4V in different initial states: (**a**,**b**) as-cast ingot, (**c**,**d**) β-forged billet, and (**e**,**f**) α + β-forged billet.

## 4. Results and Discussion

### *4.1. Microstructures of Ti-6Al-4V in Different Initial States*

The initial macro- and microstructures of the as-cast ingot, β-forged billet, and α + β-forged billet are shown in Figure 2a–f. The as-cast Ti-6Al-4V ingot exhibits a typical Widmanstätten basket-weave structure composed of coarse α lamellae (5.8 ± 2.0 μm) within prior β grains on the millimeter scale (Figure 2a,b), reflecting solidification-induced heterogeneity. Following β forging, significant refinement of the prior β grains is observed, with an average size of 642 ± 122 μm (Figure 2c). The corresponding microstructure consists of thinner α lamellae (3.0 ± 0.4 μm), indicating enhanced microstructural homogenization during deformation (Figure 2d). Further thermomechanical processing in the α + β-phase region leads to additional grain refinement, reducing the prior β grain size to 399 ± 109 μm

(Figure 2e). This condition promotes the formation of a more stable microstructure characterized by equiaxed α embedded in a transformed β matrix (Figure 2f). These results highlight the progressive microstructural evolution from coarse lamellar microstructures in the as-cast state to refined lamellar and partially equiaxed ones after thermomechanical processing, which is expected to significantly influence subsequent deformation behavior and processability.

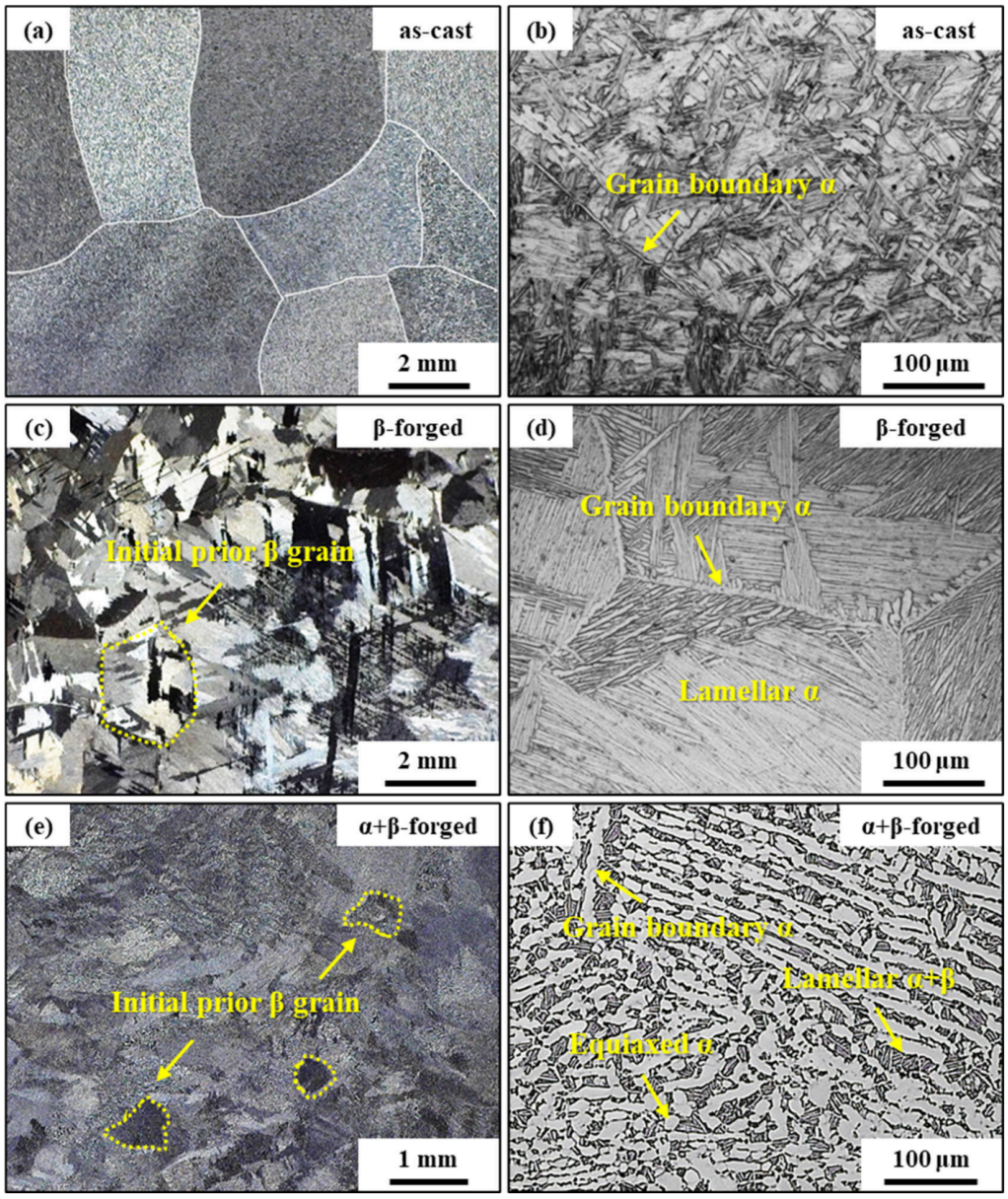



**Figure 2.** Initial macro- and microstructures of the Ti-6Al-4V in different initial states: (**a**,**b**) as-cast ingot, (**c**,**d**) β-forged billet, and (**e**,**f**) α + β-forged billet, where (**a**,**c**,**e**) show macrostructures and (**b**,**d**,**f**) show microstructures.

### *4.2. Stress–Strain Behavior and Temperature Evolution of Ti-6Al-4V in Different Initial States*

The stress–strain response during hot deformation reflects the intrinsic coupling between flow behavior and microstructural and thermal evolution, providing critical insight into the governing deformation mechanisms and microstructural changes. For reliable interpretation of hot deformation behavior, it is essential to employ isothermal flow stress ($\sigma_{iso}$) in which the influence of adiabatic heating is minimized [23].

In this study, the hot deformation behavior of Ti-6Al-4V was systematically analyzed for three different initial states: as-cast ingot, β-forged billet, and α + β-forged billet. The deformation behavior was evaluated by comparing the experimental flow stress ($\sigma_{non\text{-}iso}$) with the ANN-corrected isothermal flow stress ($\sigma_{iso}$). The analysis for the β-forged and α + β-forged billets was conducted over a temperature range of 700–1000 °C and strain rates of 0.01–10 $s^{-1}$ (Figures 3 and 4), while the as-cast ingot was examined over a higher temperature range of 900–1200 °C, with the corresponding results provided in the Supplementary Material (Figure S1). The corrected curves consistently preserve the expected thermally activated deformation characteristics, namely decreasing flow stress with increasing temperature and increasing flow stress with increasing strain rate, while eliminating the artificial softening caused by adiabatic heating at high strain rates.

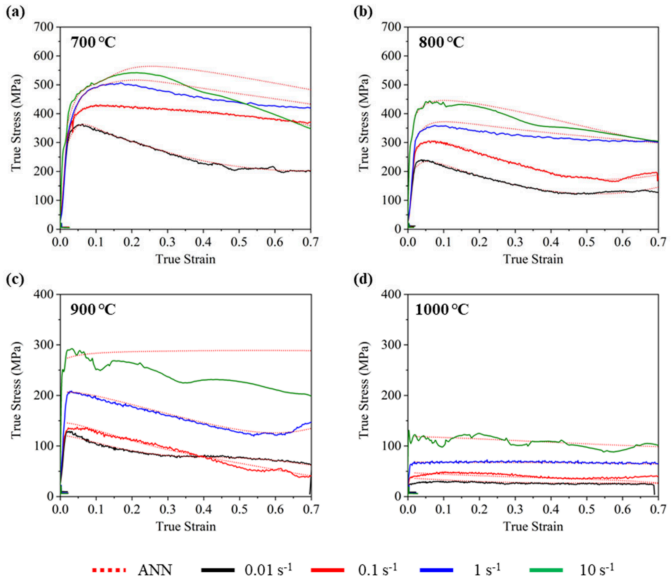



**Figure 3.** Flow stress curves of βforged billet during isothermal compression at (**a**) 700 °C, (**b**) 800 °C, (**c**) 900 °C, and (**d**) 1000 °C.

The difference between $\sigma_{non\text{-}iso}$ and $\sigma_{iso}$ arises from variations in instantaneous temperature ($T_{instant}$) during deformation, as illustrated in Figures 5 and 6 for the β-forged and α + β-forged billets, respectively, while the corresponding results for the as-cast ingot are provided in the Supplementary Material (Figure S2). At lower strain rates (0.01 and 0.1 $s^{-1}$), $T_{instant}$ remains close to the target temperature ($T_{target}$), as sufficient time is available for heat dissipation throughout the specimen. In contrast, at higher strain rates (1 and 10 $s^{-1}$), limited heat transfer results in a significant increase in $T_{instant}$. This deviation from $T_{target}$ is attributed to adiabatic heating, which becomes more pronounced with increasing strain rate. Consequently, the experimentally measured flow stress tends to underestimate the true isothermal response under high-strain-rate conditions, emphasizing the necessity of ANN-assisted correction. The flow stress exhibits typical thermally activated deformation characteristics, decreasing with increasing temperature and increasing with strain rate across all initial states. Under low-temperature and high-strain-rate conditions, strain hardening dominates due to rapid dislocation accumulation, leading to a sharp increase in flow stress up to a peak value [24]. With further deformation, dynamic softening mechanisms become active, resulting in a gradual decrease in flow stress.

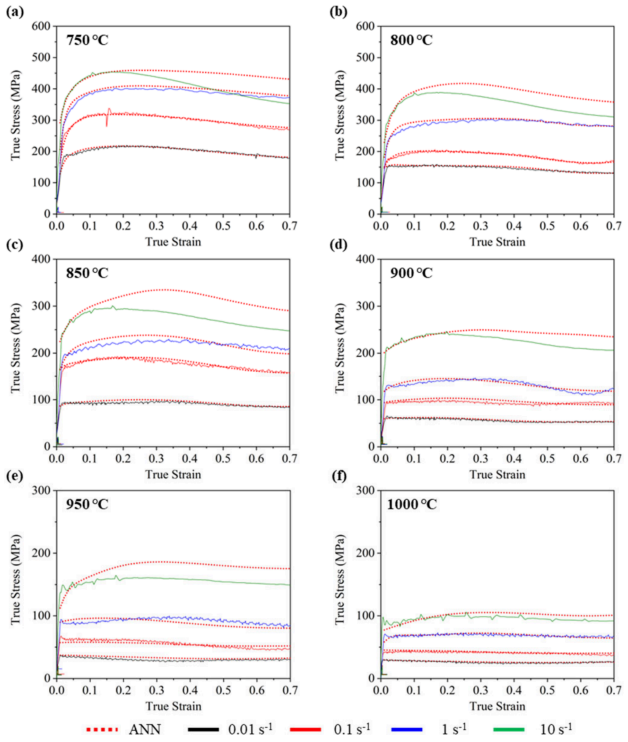



**Figure 4.** Experimental and ANN-corrected flow stress curves of α + β-forged billet at (**a**) 750 °C, (**b**) 800 °C, (**c**) 850 °C, (**d**) 900 °C, (**e**) 950 °C, and (**f**) 1000 °C.

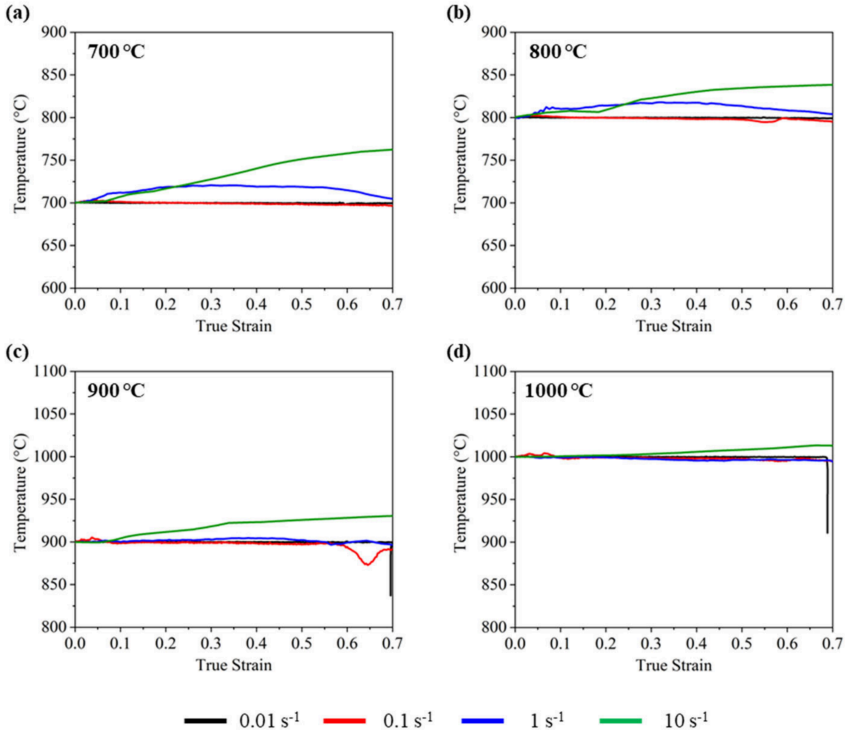



**Figure 5.** Instantaneous temperature profiles of β-forged billet during hot deformation at (**a**) 700 °C, (**b**) 800 °C, (**c**) 900 °C, and (**d**) 1000 °C.

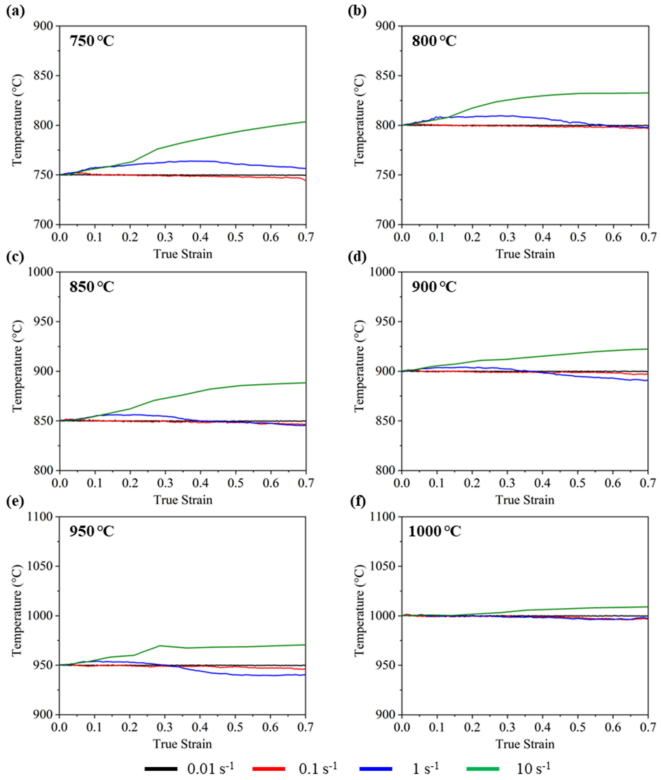



**Figure 6.** Instantaneous temperature profiles of α + β-forged billet during hot deformation at (**a**) 750 °C, (**b**) 800 °C, (**c**) 850 °C, (**d**) 900 °C, (**e**) 950 °C, and (**f**) 1000 °C.

At lower strain rates, flow softening proceeds in a stable manner, which is associated with DRV and DRX that progressively restore the microstructure. In contrast, at higher strain rates (>0.1 $s^{-1}$), the flow curves exhibit oscillatory behavior, indicating the onset of deformation instability such as strain localization or microcrack initiation [25]. This behavior becomes more pronounced at elevated temperatures (>800 °C), where discontinuous yielding is frequently observed. Such discontinuities are attributed to the rapid generation and motion of dislocations at grain boundaries, along with their interactions during deformation [23]. Although the overall deformation trends are similar across the three initial states, the as-cast ingot exhibits relatively higher deformation resistance and instability at lower temperatures due to its coarse and heterogeneous microstructure. In contrast, the β-forged and α + β-forged billets show progressively improved deformation stability, which can be attributed to the refinement and homogenization of prior β grains and α-phase morphology during thermomechanical processing. The reduction in flow stress during deformation is governed by the combined effects of adiabatic heating, DRV, DRX, and localized deformation [26]. Therefore, the observed flow behavior results from the competition between hardening and softening mechanisms controlled by both thermal and microstructural factors. For the α + β-forged billet, a decrease in $T_{instant}$ below $T_{target}$ was observed in certain cases (Figure 6c–f), which is likely associated with experimental uncertainties. Nevertheless, these deviations were effectively corrected using the ANN model, ensuring consistent and reliable estimation of $\sigma_{iso}$ across the entire deformation range. It should be noted that interpretation of deformation mechanisms based solely on flow curve characteristics is inherently limited. Therefore, to achieve a more comprehensive understanding of deformation behavior and stability, processing maps for Ti-6Al-4V in the as-cast ingot, β-forged billet, and α + β-forged billet are analyzed in detail in the following section.

*4.3. Processing Map-Guided Design of Thermomechanical Conditions for Filler Wire Fabrication*

Processing maps were developed to identify optimal thermomechanical conditions that enable microstructural control while avoiding flow instability and defect formation during hot deformation. The maps were constructed based on the dynamic materials model (DMM) proposed by Prasad et al. [27], which considers the workpiece as a dissipater of the applied power during deformation. The efficiency of power dissipation (η), representing the fraction of power dissipated through microstructural evolution, is defined as:

$$\eta = \frac{2m}{m+1} \tag{1}$$

where m is the strain rate sensitivity, expressed as:

$$m = \frac{dlog\sigma}{dlog(\dot{\varepsilon})} \tag{2}$$

The variation of η as a function of temperature and strain rate constitutes the power dissipation map, which reflects the domains of distinct microstructural mechanisms. To identify unstable deformation regions, the instability parameter (ξ) is defined as [28]:

$$\xi(\dot{\varepsilon}) = \frac{\partial \log\left(\frac{m}{m+1}\right)}{\partial log(\dot{\varepsilon})} + m < 0 \tag{3}$$

Regions where $\xi(\dot{\varepsilon}) < 0$ correspond to flow instability, which is typically associated with localized deformation or shear band formation and should therefore be avoided during processing. The final processing map is obtained by superimposing the instability map onto the power dissipation map. To ensure high-resolution mapping, the experimental dataset covering a wide range of temperatures and strain rates was further refined using the ANN model, allowing accurate interpolation of flow stress data. The efficiency of power dissipation and instability domains were calculated using Equations (1) and (3), respectively. The resulting processing maps at a strain of 0.6 are shown in Figure 7a–c for the as-cast ingot, β-forged billet, and α + β-forged billet, respectively. The contour values represent η, while the shaded regions indicate flow instability. In hot deformation, strain acts as a driving force for recrystallization, and higher strain levels generally promote DRX [29]. For the β-forged and α + β-forged billets, high-efficiency domains were identified in the temperature range of 900–950 °C at relatively high strain rates (1–10 $s^{-1}$), indicating optimal processing windows. These domains are typically associated with DRX- or DRV-dominated deformation, leading to improved microstructural refinement and deformation stability. In contrast, instability regions correspond to unfavorable deformation modes such as flow localization and should be excluded from process design. Previous studies by Zhang et al. [18] and Quan et al. [30] reported optimal deformation conditions for Ti-6Al-4V in the range of 850–950 °C with relatively low strain rates, depending on the initial microstructure. In comparison, the present results suggest that stable deformation can also be achieved at higher strain rates when appropriate thermomechanical conditions are selected. For the as-cast ingot, the optimal domain was identified near 1100 °C within the β-phase region (Figure 7a), reflecting the need for higher temperatures to accommodate the coarse and heterogeneous initial microstructure. In contrast, both β-forged and α + β-forged billets exhibited optimal domains near 920 °C, where enhanced deformation stability and microstructural refinement are achieved.

Based on the processing map analysis, the as-cast ingot exhibited the highest power dissipation efficiency within the stable β-phase region at approximately 1100 °C. However, for the present study, the processing temperature was intentionally selected at 920 °C

within the α + β-phase region under a high-strain-rate region. Although 920 °C does not correspond to the maximum power dissipation efficiency, it lies within a stable processing domain and, more importantly, within the dynamic recrystallization region, where significant grain refinement can be achieved during hot deformation. The combined effects of dynamic recrystallization and phase transformation promote the formation of a refined and homogeneous α microstructure, leading to improved workability and mechanical performance. Processing under these conditions promotes stable plastic deformation and effective microstructural refinement, enabling the production of high-quality filler wire directly from the as-cast ingot. Consequently, the conventional β- and α + β-forging steps can be eliminated without compromising process stability or the final mechanical performance. However, it should be noted that a single 50% height reduction is insufficient to achieve a fully uniform microstructure in the as-cast ingot. The processing map serves as a design tool to determine the optimal deformation domain under high-strain-rate conditions relevant to rolling. The applicability of the selected condition to filler wire fabrication was further evaluated through hot-rolling experiments, providing insight into the microstructural evolution and process feasibility during direct conversion from the as-cast ingot.

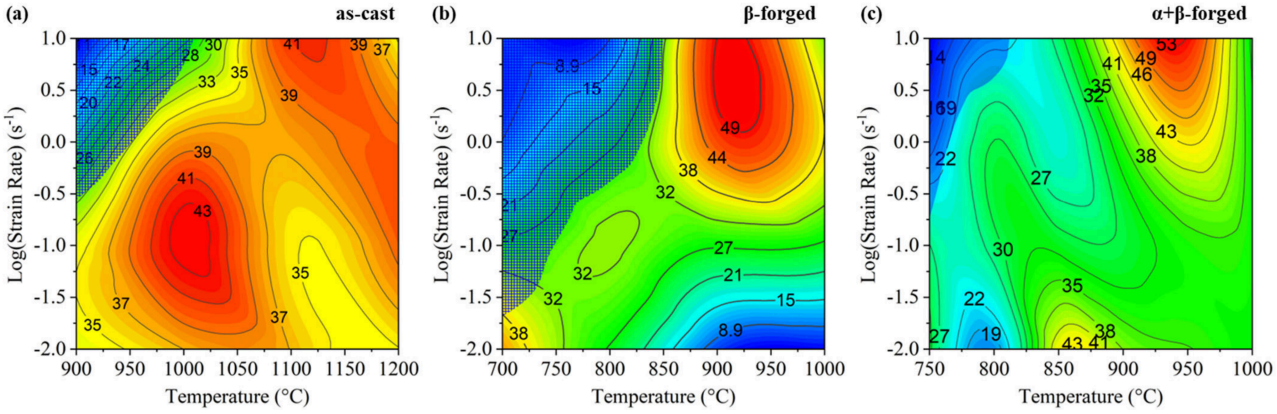



**Figure 7.** Processing maps of Ti-6Al-4V at a strain of 0.6 for different initial states: (**a**) as-cast ingot, (**b**) β-forged billet, and (**c**) α + β-forged billet.

### *4.4. Microstructural Evolution of Ti-6Al-4V in Different Initial States*

#### 4.4.1. Microstructural Evolution of As-Cast Ingot During Hot Deformation

The microstructural evolution of Ti-6Al-4V during hot deformation is strongly governed by deformation temperature, strain rate, and strain, which collectively determine the dominant restoration mechanisms and phase transformations [28]. Figure 8 shows the optical microstructures of the as-cast ingot deformed within the β-phase region and subsequently water-quenched. The microstructure consists of the martensitic α′ phase transformed from the high-temperature β-phase, reflecting rapid cooling. In addition, a well-developed β subgrain structure is observed within the prior β grains (Figure 8a–f). The prior β grain boundaries and subgrain boundaries are indicated by solid black lines and yellow dashed lines, respectively. At higher strain rates (e.g., $\geq$1 $s^{-1}$), the β grains exhibit pronounced elongation normal to the deformation direction (Figure 8c,f), indicating deformation-induced anisotropy. The formation of subgrain boundaries within the deformed β grains suggests that DRV is the dominant restoration mechanism under these conditions. This observation is consistent with the findings of Poletti et al. [31], who reported that DRV governs microstructural evolution in Ti-6Al-4V deformed in the β-phase region through the formation of subgrain structures.

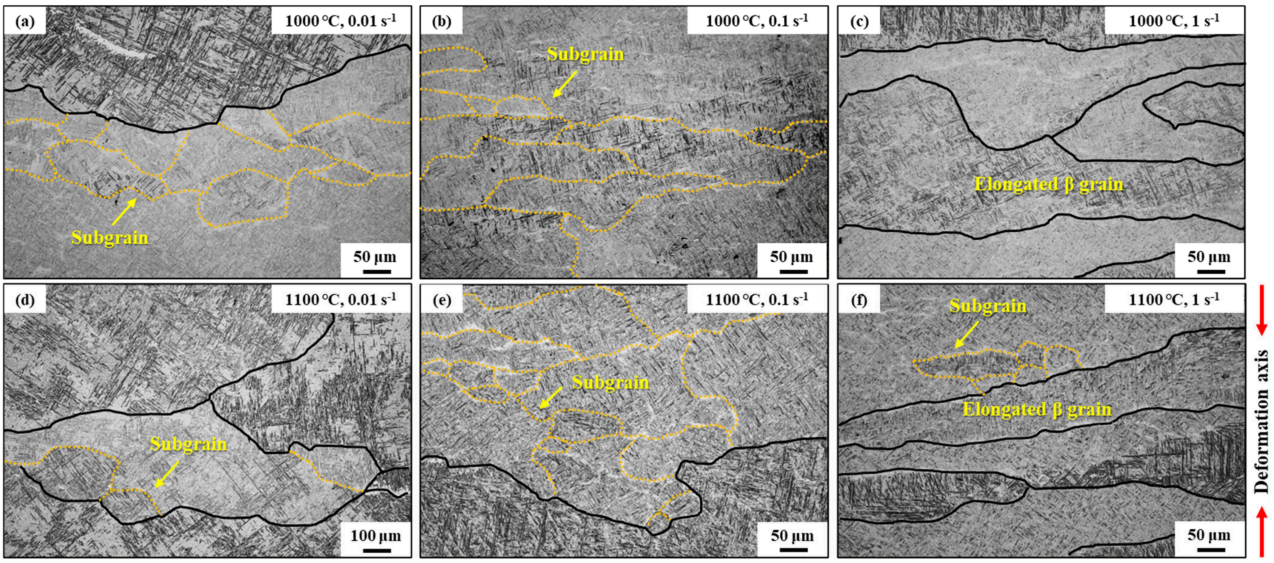



**Figure 8.** Optical microstructures of as-cast ingot after deformation in the stable domains of the processing map: (**a**) 1000 °C, 0.01 $s^{-1}$, (**b**) 1000 °C, 0.1 $s^{-1}$, (**c**) 1000 °C, 1 $s^{-1}$, (**d**) 1100 °C, 0.01 $s^{-1}$, (**e**) 1100 °C, 0.1 $s^{-1}$, and (**f**) 1100 °C, 1 $s^{-1}$.

The EBSD inverse pole figure (IPF) map of the as-cast ingot deformed in the α + β-phase region is shown in Figure 9a. The microstructure contains fine equiaxed grains; however, grain morphology alone is insufficient to distinguish between DRV and DRX. Therefore, misorientation analysis was employed [32]. High-angle grain boundaries (HAGBs, $\theta \geq 15°$) and low-angle grain boundaries (LAGBs, $2° \leq \theta < 15°$) are distinguished to identify the dominant deformation mechanisms. In the EBSD maps used in this study, HAGBs with $\theta \geq 15°$ were represented in black, and LAGBs with $2° \leq \theta < 5°$ and $5° \leq \theta < 15°$ were represented in yellow and orange, respectively. DRV is typically characterized by subgrain formation within elongated grains, whereas DRX produces fine equiaxed grains bounded by HAGBs. The EBSD results indicate the presence of localized DRX, where fine equiaxed grains form preferentially along prior β grain boundaries, resulting in a necklace-type structure. This behavior is attributed to the accumulation of dislocations during plastic deformation, where insufficient heat dissipation leads to stored energy that promotes DRX nucleation [33].

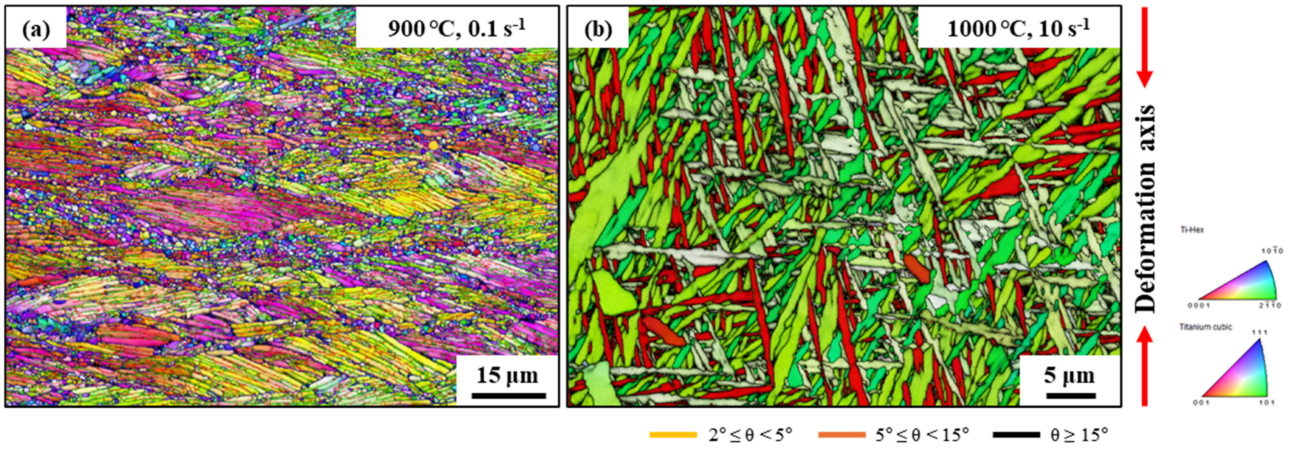



**Figure 9.** EBSD IPF maps of as-cast ingot deformed at (**a**) 900 °C, 0.1 $s^{-1}$ and (**b**) 1000 °C, 10 $s^{-1}$.

However, the heterogeneous distribution of DRX grains suggests incomplete recrystallization. For subsequent wire drawing, a homogeneous equiaxed microstructure is

preferred to ensure adequate ductility and formability. These observations indicate that a single 50% height reduction in the α + β-phase region alone is generally insufficient to convert the as-cast ingot into a wire with a fully uniform microstructure. This result highlights that the total applied strain is a critical parameter governing microstructural homogeneity. Consequently, two practical approaches can be considered to address this limitation. First, an initial deformation step in the β-phase region can be introduced to effectively break down coarse prior β grains, followed by subsequent deformation in the α + β region to promote uniform DRX. The effectiveness of this approach is supported by the microstructure obtained after deformation in the β-phase region (Figure 9b), which exhibits a refined basket-weave structure composed of fine α lamellae, confirming its role in enhancing microstructural refinement. Alternatively, microstructural uniformity may be achieved by applying a greater total strain directly within the α + β region. The latter approach is also supported by previous studies on Ti-6Al-4V, which have shown that the globularization of the α phase is strongly dependent on accumulated strain. For instance, it has been reported that only partial spheroidization occurs at a strain of ~1.0, whereas near-complete globularization can be achieved at a higher strain of ~1.4 under similar thermomechanical conditions [34]. These findings clearly demonstrate that sufficient strain accumulation is essential for achieving a homogeneous and refined microstructure. Considering the objective of this study to develop a cost-effective manufacturing route, the second approach, namely increasing the total strain within the α + β region, offers a more practical and industrially attractive solution by eliminating the need for additional β-region processing steps.

#### 4.4.2. Microstructural Evolution of β-Forged Billet During Hot Deformation

The microstructural evolution of the β-forged billet was systematically analyzed in relation to the processing map, considering both stable and unstable deformation domains. Figure 10 shows the combined image quality (IQ)-IPF maps of the β-forged billet samples deformed under representative processing conditions at various temperatures and strain rates. The combined IQ-IPF maps were employed to simultaneously visualize crystallographic orientation and morphology-related contrast, enabling clearer identification of fine equiaxed grains, elongated grains, and local deformation heterogeneity than an IPF map alone. The microstructure consists of a mixture of fine equiaxed grains and elongated grains, indicating the coexistence of DRX and DRV mechanisms. Newly formed grains are predominantly observed along prior grain boundaries (Figure 10a–f), suggesting boundary-mediated recrystallization. The fractions of HAGBs and LAGBs vary depending on the deformation condition. The quantitative boundary fraction data are summarized in Table 2. Fine equiaxed grains bounded by HAGBs correspond to DRX, whereas elongated grains containing LAGBs represent DRV-dominated regions. At elevated temperatures (e.g., 1000 °C), the fraction of HAGBs increases significantly (Figure 10e,f), indicating enhanced recrystallization due to increased atomic mobility and grain boundary migration. These observations confirm that deformation within the high-efficiency domains of the processing map promotes DRX and/or DRV, resulting in stable flow behavior and improved workability.

In contrast, Figure 11 shows distinct deformation-induced defects and instability mechanisms in the microstructures deformed in the instability domains. Flow localization is observed at lower temperatures and moderate-to-high strain rates (e.g., 700 °C, 0.1–10 $s^{-1}$ and 800 °C, 1 $s^{-1}$), as shown in Figure 11a,d,g,i. Additionally, kinking of α lamellae is evident at similar temperatures and strain rates (Figure 11b,e,h,j,k), indicating instability in lamellar α structures. Microvoid formation is also detected at 700 °C under low-to-moderate strain rates (e.g., 0.1 $s^{-1}$ and 1 $s^{-1}$), as shown in Figure 11c,f. This feature is

attributed to strain incompatibility and stress concentration at grain boundaries [26]. These instability features are detrimental to mechanical integrity and must therefore be avoided during thermomechanical processing such as rolling or forging. Overall, although the β-forged billet exhibits improved deformation stability compared to the as-cast ingot, deformation instability can still develop under unfavorable processing conditions.

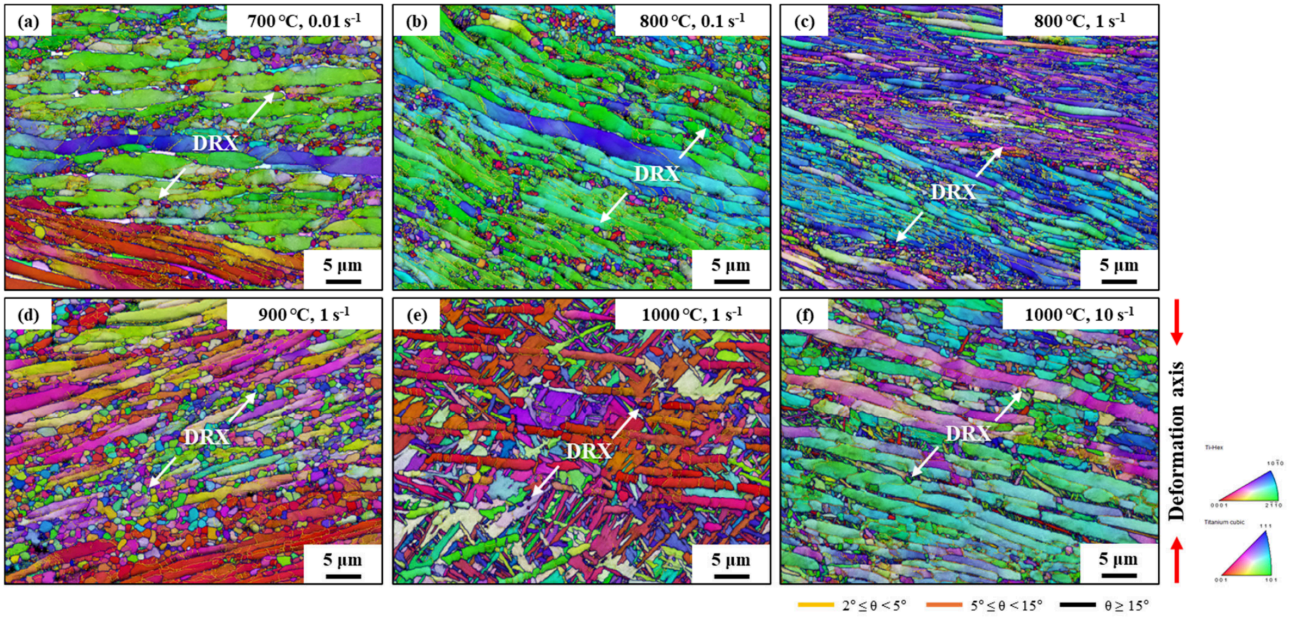



**Figure 10.** EBSD combined IQ-IPF maps of β-forged billet deformed under different domains of the processing map: (**a**) 700 °C, 0.01 $s^{-1}$, (**b**) 800 °C, 0.1 $s^{-1}$, (**c**) 800 °C, 1 $s^{-1}$, (**d**) 900 °C, 1 $s^{-1}$, (**e**) 1000 °C, 1 $s^{-1}$, and (**f**) 1000 °C, 10 $s^{-1}$.

**Table 2.** Fractions of LAGBs and HAGBs in the β-forged billet deformed under different hot-deformation conditions.

| Initial State | Temperature (°C) | Strain Rate ($s^{-1}$) | LAGB Fraction (%) | HAGB Fraction (%) |
|---|---|---|---|---|
| β-forged billet | 700 | 0.01 | 49.1 | 50.9 |
| | 800 | 1 | 50.3 | 49.7 |
| | 800 | 0.1 | 49.3 | 50.7 |
| | 900 | 1 | 37.7 | 62.3 |
| | 1000 | 1 | 14.0 | 86.0 |
| | 1000 | 10 | 36.6 | 63.4 |

4.4.3. Microstructural Evolution of α + β-Forged Billet During Hot Deformation

Figure 12 shows the EBSD IPF maps of the α + β-forged billet deformed within the stable domains of the processing map (Figure 7c). The microstructure is characterized by deformed α grains containing fine substructures, along with serrated grain boundaries (Figure 12a–c) [35]. The substructured grains exhibit an average size of approximately 0.8 ± 0.3 μm and are nearly equiaxed, indicating significant refinement. The presence of serrated boundaries suggests active grain boundary migration during deformation. At 900 °C and a high strain rate (10 $s^{-1}$), a uniformly distributed equiaxed α microstructure is observed throughout the matrix (Figure 12c), with an average grain size of 5.2 ± 3.1 μm. This condition corresponds closely to the high-efficiency domain identified in the processing map, indicating that DRX is highly active under this condition. The enhanced refinement observed in the α + β-forged billet can be attributed to the prior β forging followed by

α + β forging, which promotes the progressive breakdown of lamellar structures and facilitates recrystallization during subsequent deformation. This demonstrates that sequential thermomechanical processing is highly effective in achieving microstructural homogeneity and grain refinement. At higher deformation temperatures (e.g., 950 °C), the microstructure consists of equiaxed α grains embedded within a transformed β matrix (Figure 12d,e). This behavior is associated with deformation near the β-transus temperature, where a local temperature rise due to adiabatic heating (Figure 6e) promotes phase transformation and reduces the stability of the α phase. Overall, these results provide strong experimental evidence supporting the effectiveness of the two-stage β → α + β thermomechanical processing route in producing a refined and homogeneous microstructure, which is favorable for stable deformation behavior and subsequent forming processes. However, it should be noted that such multi-step processing inherently involves additional thermomechanical operations, which increase manufacturing complexity and cost. Therefore, although this approach represents a robust and conventional strategy for microstructural control, it is not fully aligned with the objective of this study, which aims to develop a simplified and cost-effective direct manufacturing route from the as-cast ingot.

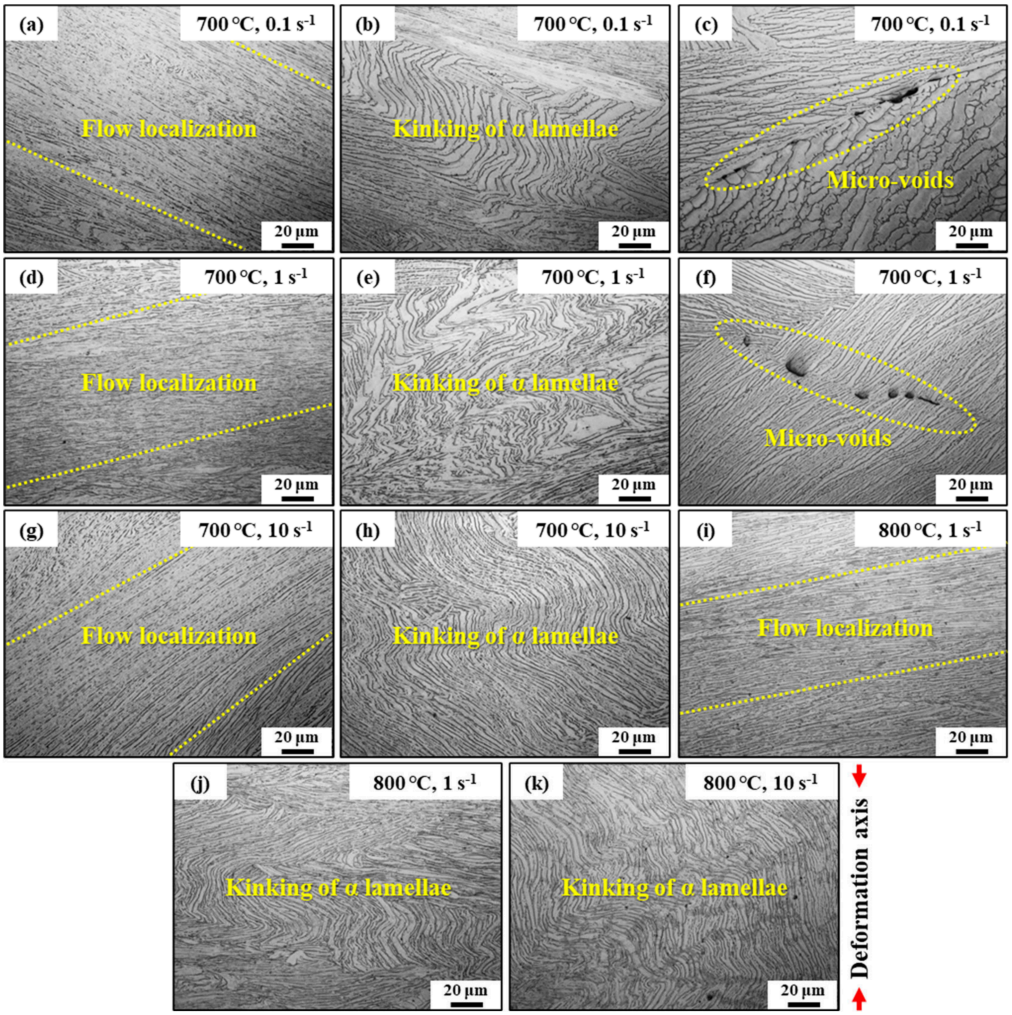



**Figure 11.** Optical microstructures of β-forged billet after hot deformation at (**a**–**c**) 700 °C, 0.1 $s^{-1}$, (**d**–**f**) 700 °C, 1 $s^{-1}$, (**g**,**h**) 700 °C, 10 $s^{-1}$, (**i**,**j**) 800 °C, 1 $s^{-1}$, and (**k**) 800 °C, 10 $s^{-1}$.

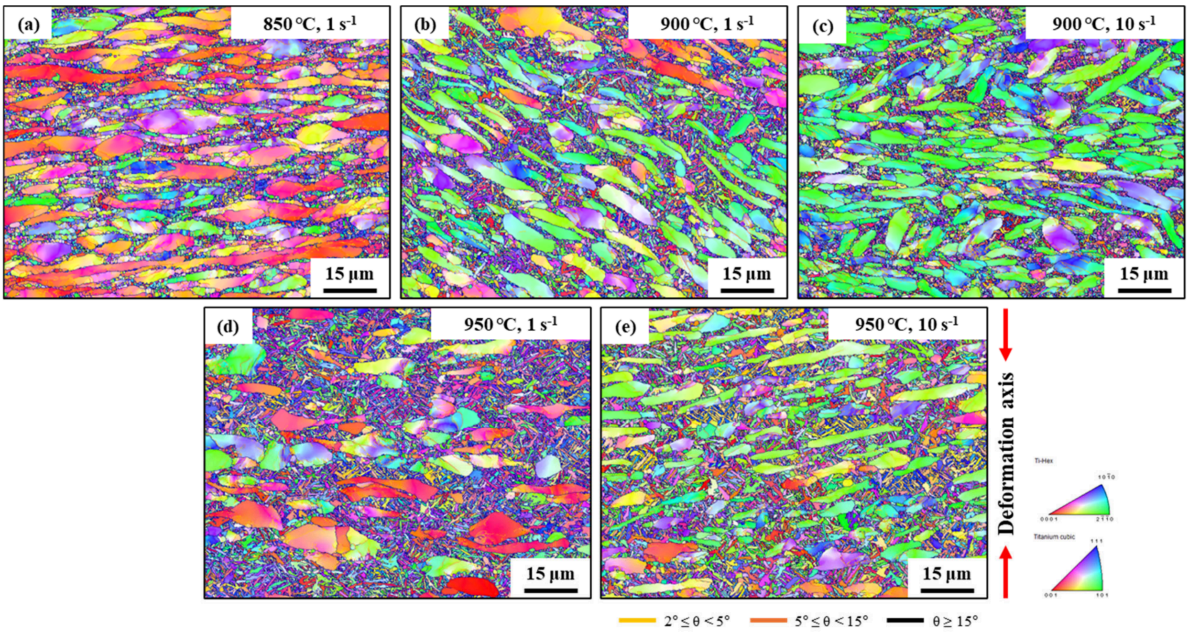



**Figure 12.** EBSD IPF maps of α + β-forged billet deformed under representative domains of the processing map: (**a**) 850 °C, 1 $s^{-1}$, (**b**) 900 °C, 1 $s^{-1}$, (**c**) 900 °C, 10 $s^{-1}$, (**d**) 950 °C, 1 $s^{-1}$, and (**e**) 950 °C, 10 $s^{-1}$.

### *4.5. Wire Fabrication Procedure and Microstructure*

#### 4.5.1. Processing Map-Guided Wire Fabrication Procedure

In this study, a processing map-guided thermomechanical design strategy was established and subsequently validated through practical wire fabrication. More importantly, this section aims to experimentally demonstrate the feasibility of a cost-effective direct processing route from the as-cast ingot. Based on the stable deformation domain identified in the processing map (Figure 7), an optimum condition near 920 °C under high-strain-rate deformation was selected as the core processing parameter. To evaluate the robustness and industrial applicability of this design strategy, filler wires were fabricated from three different initial states: as-cast ingot, β-forged billet, and α + β-forged billet, as illustrated in Figure 13. Both forged billets were intentionally included as benchmark cases representing conventional thermomechanical processing routes.

The β-forged billet was produced by hot forging the as-cast ingot in the β-phase region (1140 °C) to fragment coarse prior β grains, while the α + β-forged billet was prepared by secondary forging in the α + β-phase region (920 °C) to transform α lamellae into equiaxed α grains. While these pre-processed billets reflect established industrial practices, the primary objective of this study is to verify whether comparable results can be achieved through direct processing of the as-cast ingot under optimized conditions. Cylindrical bars (Φ12 mm) were machined from each initial state, and multi-step groove rolling was performed at 920 °C following the processing map design (Figure 7). The diameter was reduced to Φ2.8 mm, followed by a stress-relief heat treatment at 600 °C for 2 h. Final wire drawing was then conducted to obtain a Φ1.7 mm filler wire, thereby completing full-scale validation from process design to final product, as shown in Figure 13.

Hot-rolling of Ti-6Al-4V presents practical challenges, including oxidation, surface folding, and strong strain rate sensitivity. To mitigate these issues, samples were coated with Bonderite L-GP 12 and Delta Glaze (LGF 151) prior to deformation. Surface folding was minimized by optimizing inter-groove spacing to maintain geometric stability, while a high strain rate (~10 $s^{-1}$), consistent with the processing map prediction, was employed to ensure deformation stability. After rolling, surface coatings were removed by sandblasting

and chemical pickling in a solution of 2% hydrofluoric acid + 20% nitric acid + 78% DI water, prepared in accordance with ASTM B600 [36], resulting in clean and defect-free wire surfaces suitable for WAAM applications.

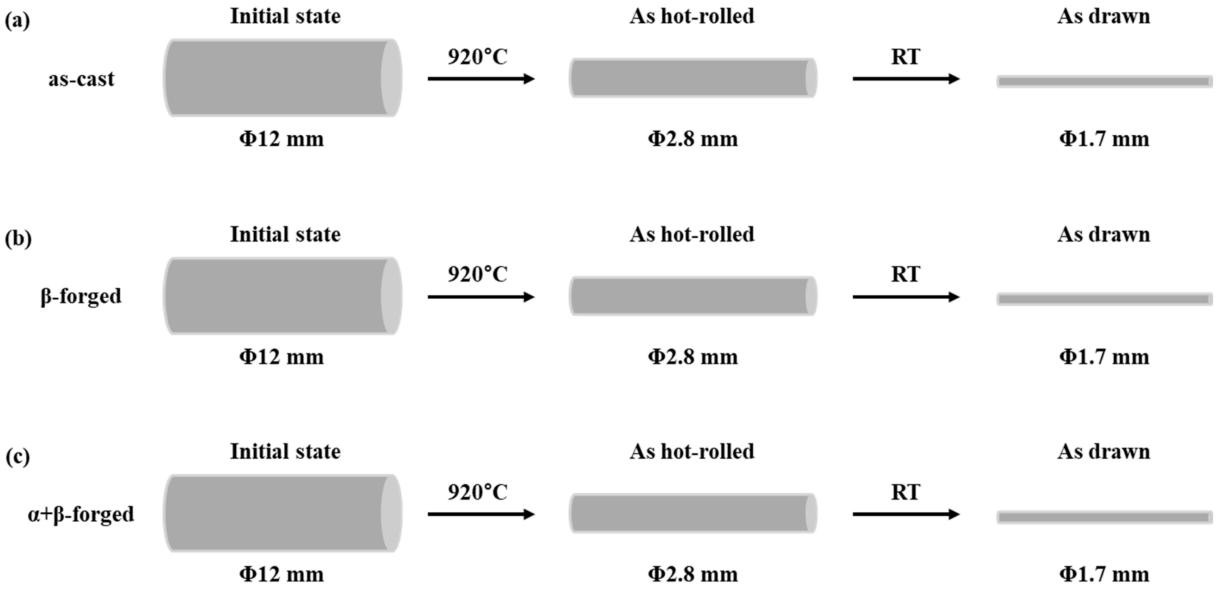



**Figure 13.** Schematic illustration of filler wire fabrication routes for Ti-6Al-4V from different initial states: (**a**) as-cast ingot, (**b**) β-forged billet, and (**c**) α + β-forged billet, followed by hot-rolling at 920 °C and room-temperature wire drawing.

#### 4.5.2. Microstructural Evolution During Hot-Rolling and Room-Temperature Drawing

To elucidate the underlying deformation mechanisms and validate the processing map-guided design, microstructural evolution during hot-rolling and room-temperature drawing was systematically analyzed using EBSD along the transverse direction (TD). Figure 14 shows the EBSD microstructures of the wires fabricated from different initial states after hot-rolling and room-temperature drawing. The as-cast ingot initially exhibits coarse prior β grains with a basket-weave α lamellar structure (α-lamella thickness: 1.0 ± 0.4 μm, Figure 14a). Under the processing map-guided rolling condition at 920 °C, these lamellae are effectively fragmented into equiaxed α grains (5.7 ± 2.4 μm, Figure 14b), indicating that DRV and DRX mechanisms are actively involved even in the coarse as-cast microstructure. This behavior is consistent with previous studies reporting that thin α lamellae tend to fragment into fine equiaxed α grains, whereas thicker lamellae are more prone to kinking and elongation during hot deformation [37]. This microstructural evolution can be further rationalized in terms of accumulated strain. Previous studies on Ti-6Al-4V have demonstrated that the globularization of lamellar α is strongly dependent on strain, where only partial spheroidization occurs at a strain of ~1.0, while near-complete globularization is achieved at higher strains exceeding ~1.4 [34]. In this study, the hot-rolling process reduces the bar diameter from Φ12 mm to Φ2.8 mm, corresponding to a true strain of ~2.9. This strain level significantly exceeds the threshold required for effective globularization, thereby providing sufficient driving force for microstructural refinement and homogenization. These results clearly indicate that the second approach proposed in this study, namely achieving microstructural uniformity through increased total strain within the α + β-phase region, is not only theoretically valid but also practically realized in the current processing route. The substantial strain accumulation during multi-step rolling enables effective breakdown of the initial coarse lamellar structure, eliminating the necessity for additional β-region deformation steps.

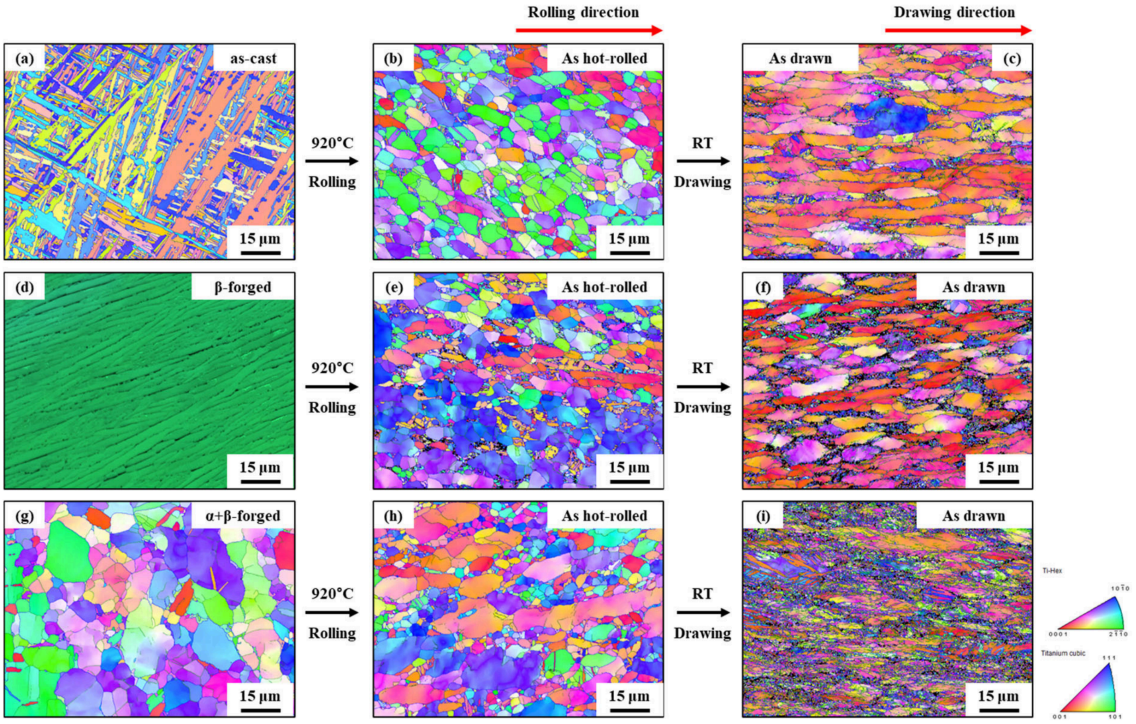



**Figure 14.** EBSD IPF maps of the Ti-6Al-4V in different initial states: (**a**–**c**) as-cast ingot, (**d**–**f**) β-forged billet, and (**g**–**i**) α + β-forged billet, showing microstructural evolution after hot-rolling at 920 °C and subsequent room-temperature wire drawing.

For the β-forged billet, the initially refined lamellar structure (2.4 ± 0.5 μm) is further transformed into a relatively homogeneous equiaxed α microstructure (5.6 ± 2.5 μm, Figure 14e). However, this microstructure does not show a significant advantage over that obtained from the as-cast ingot under the optimized processing route, suggesting that the contribution of prior β-forging becomes less critical when sufficient strain is applied during hot-rolling. In the α + β-forged billet, the pre-existing equiaxed α grains evolve into a mixed grain-size distribution due to localized dynamic recrystallization during multi-step rolling (Figure 14h), reflecting heterogeneous strain accumulation. Such behavior is consistent with previous studies indicating that localized strain partitioning promotes fine grain formation in high-strain regions while relatively coarser grains are retained in low-strain regions [38,39]. Although this route yields a refined microstructure, it requires additional thermomechanical steps. After room-temperature drawing, all samples exhibit deformation-induced alignment of α phases (Figure 14c,f,i). The wire fabricated from the as-cast ingot shows predominantly elongated α features, whereas the wires fabricated from the β-forged and α + β-forged billets exhibit more fragmented and refined α structures. Nevertheless, all wires fabricated from different initial states exhibit a homogeneous and defect-free final microstructure. Overall, these results demonstrate that sufficient strain accumulation during processing plays a more dominant role than the initial microstructure in determining the final microstructural state. This finding provides strong experimental support for the feasibility of direct processing from the as-cast ingot, aligning with the objective of developing a simplified and cost-effective manufacturing route.

#### 4.5.3. Texture Evolution

Texture evolution was analyzed to correlate crystallographic behavior with processing map-guided deformation mechanisms. Figure 15 shows the pole figures of the final wires after room-temperature drawing. In the pole figures, the horizontal direction corresponds to the drawing direction (DD), and the vertical direction corresponds to the transverse

direction (TD). Based on this coordinate system, all wires exhibit a strong fiber texture with a pronounced <0001>-related component after room-temperature drawing, which is consistent with deformation accompanied by strong crystallographic alignment in α-Ti alloys [40,41]. The wire fabricated from the as-cast ingot exhibits relatively moderate texture intensity, whereas the wires fabricated from the β-forged and α + β-forged billets show progressively stronger <0001> alignment. The grains with different crystallographic orientations exhibit different slip activity and stored deformation energy, resulting in variations in dynamic recovery (DRV) and dynamic recrystallization (DRX) behavior. This difference is attributed to the presence of finer and more uniformly distributed equiaxed α grains, which facilitate strain partitioning and enhance crystallographic alignment during deformation. Importantly, this result indicates that processing map-guided deformation not only ensures microstructural stability but also promotes predictable texture evolution. Such control is particularly critical for WAAM feedstock, where crystallographic anisotropy can significantly influence deposition behavior, residual stress evolution, and mechanical reliability.

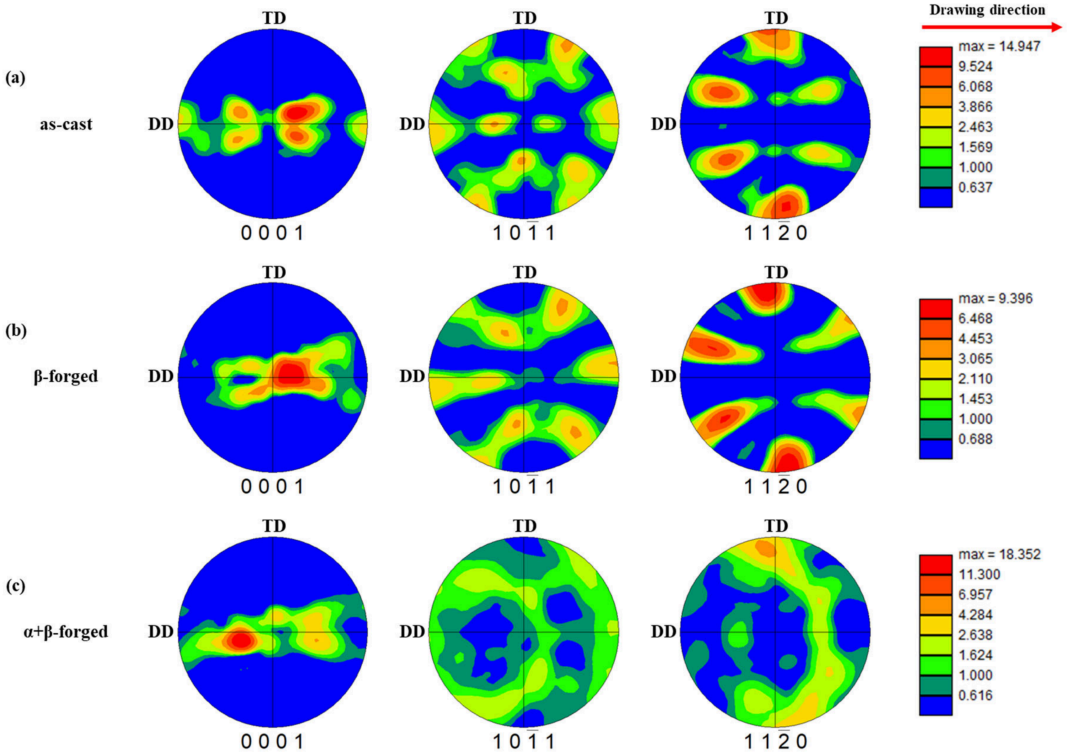



**Figure 15.** Pole figures of the final Ti-6Al-4V filler wires fabricated from different initial states: (**a**) as-cast ingot, (**b**) β-forged billet, and (**c**) α + β-forged billet. The horizontal direction corresponds to the drawing direction (DD), and the vertical direction corresponds to the transverse direction (TD).

#### 4.5.4. Tensile Properties and Limitation of Current Study

The engineering stress–strain curves of the final wires fabricated from different initial states are shown in Figure 16, and the corresponding quantitative tensile properties are summarized in Table 3. Together, these results provide critical validation of the proposed processing-map-guided design strategy. Despite differences in initial microstructure, only moderate variations in tensile properties are observed. The wire fabricated from the as-cast ingot exhibits slightly lower strength and ductility due to the partial retention of elongated α features inherited from the initial coarse microstructure. In contrast, the wires fabricated from the β-forged and α + β-forged billets show improved strength–ductility balance. Among them, the wire fabricated from the α + β-forged billet demonstrates the most

balanced tensile performance, which can be attributed to its uniformly refined equiaxed α microstructure.

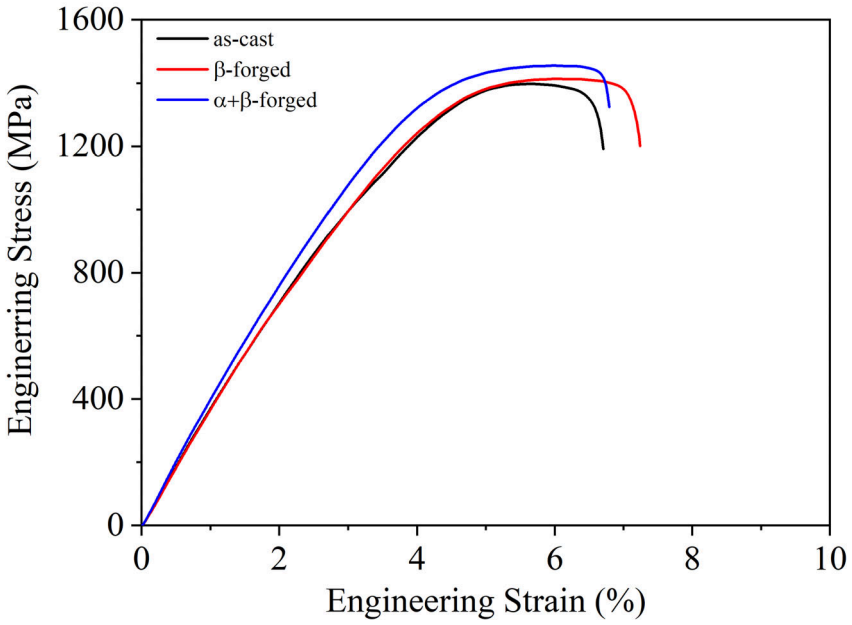



**Figure 16.** Engineering stress–strain curves of Ti-6Al-4V filler wires developed from different initial states: as-cast ingot, β-forged billet, and α + β-forged billet.

**Table 3.** Tensile properties of Ti-6Al-4V filler wires developed from different initial states.

| Initial State | Yield Strength (MPa) | Tensile Strength (MPa) | Elongation (%) |
|---|---|---|---|
| as-cast ingot | 1060 ± 21 | 1408 ± 38 | 6.7 ± 0.7 |
| β-forged billet | 1115 ± 18 | 1431 ± 28 | 7.2 ± 0.7 |
| α + β-forged billet | 1145 ± 16 | 1452 ± 32 | 6.8 ± 0.5 |

Importantly, however, the wire fabricated from the as-cast ingot exhibits tensile properties comparable to those of the wires fabricated from the forged billets. This clearly demonstrates that the processing map-guided thermomechanical design effectively mitigates the limitations associated with the initial coarse microstructure by promoting sufficient microstructural refinement and stable deformation behavior. The development of refined α morphology (Figure 14) and strong fiber texture with a pronounced <0001>-related component (Figure 15) contributes to improved deformation compatibility and more uniform strain distribution, thereby ensuring a stable strength–ductility balance across all processing routes. These results provide direct experimental validation of the processing map-guided design strategy, confirming that high-quality Ti-6Al-4V filler wire can be successfully fabricated through hot-rolling at 920 °C under high-strain-rate conditions, followed by room-temperature drawing. Most importantly, the comparative analysis demonstrates that costly and time-consuming pre-forging steps can be effectively eliminated without compromising tensile performance. This highlights that direct processing from the as-cast ingot is not only technically feasible but also economically advantageous, offering a simplified and cost-effective manufacturing route for WAAM filler wire production.

The main limitation of the present study is related to surface oxidation during hot rolling. Although a delta glaze was applied to protect the wire surface, oxidation could still occur during hot rolling due to exposure to the high-temperature environment. Consequently, the oxide/scale layer formed on the wire surface was removed by grinding before

subsequent wire drawing. While this approach was effective for laboratory-scale fabrication, it is not ideal for high-volume industrial production because additional grinding increases processing time, material loss, and production cost. Therefore, for industrial-scale manufacturing, a controlled-atmosphere hot-rolling system, such as an enclosed chamber with an Ar atmosphere, would be desirable to minimize oxidation and reduce the need for post-rolling surface treatment. Future work will focus on developing and validating such an inert-atmosphere processing system for continuous and high-volume Ti-6Al-4V filler-wire production.

## 5. Conclusions

This study established and experimentally validated a processing map-guided thermomechanical design strategy for the fabrication of Ti-6Al-4V filler wire for WAAM applications, with particular emphasis on the feasibility of direct processing from an as-cast ingot. The main conclusions are summarized as follows:

(1) The hot deformation behavior of Ti-6Al-4V was systematically characterized over a wide range of temperatures (700–1200 °C) and strain rates (0.01–10 $s^{-1}$) using specimens with three different initial states: the as-cast ingot, the β-forged billet, and the α + β-forged billet. ANN-assisted correction enabled reliable estimation of isothermal flow stress by compensating for non-isothermal effects.

(2) Processing maps constructed from the corrected data identified stable deformation domains governed by DRV and DRX, as well as instability regions associated with flow localization and microstructural damage. An optimum thermomechanical condition near 920 °C under high-strain-rate deformation was identified as a robust processing window.

(3) The validity of the processing map-guided design was confirmed through full-scale wire fabrication. Under the optimized condition, high-quality Ti-6Al-4V filler wire (Φ1.7 mm) was successfully produced via multi-step hot-rolling followed by room-temperature drawing, even when starting directly from the as-cast ingot.

(4) The multi-step rolling process introduced a large accumulated strain (~2.9), significantly exceeding the critical strain required for effective globularization of lamellar α. This high-strain level enabled substantial microstructural refinement and homogenization, demonstrating that, under the optimized thermomechanical conditions, the final microstructure is governed primarily by the imposed strain rather than the initial microstructure.

(5) All fabricated wires exhibited a strong fiber texture with a pronounced <0001>-related component, and the evolution of refined α morphology and texture contributed to stable deformation behavior and a consistent strength–ductility balance. As a result, only moderate variations in tensile properties were observed among different initial states, with the wire fabricated from the as-cast ingot showing performance comparable to the wires fabricated from the forged billets.

These results demonstrate that the conventional requirement for prior β or α + β forging can be effectively replaced by a strain-controlled thermomechanical approach within the α + β region. Consequently, the proposed strategy enables direct and cost-effective manufacturing of high-quality Ti-6Al-4V filler wire from as-cast ingots, offering a simplified and industrially attractive alternative to conventional billet-based processing routes for WAAM applications.

**Supplementary Materials:** The following supporting information can be downloaded at https://www.mdpi.com/article/10.3390/met16090950/s1, Figure S1: Flow stress curves of as-cast ingot during isothermal compression at (a) 900 °C, (b) 1000 °C, (c) 1100 °C, and (d) 1200 °C; Figure S2:

Instantaneous temperature profiles of as-cast ingot during hot deformation at (a) 900 °C, (b) 1000 °C, (c) 1100 °C, and (d) 1200 °C.

**Author Contributions:** A.K.M.: Data curation, visualization, writing—original draft. J.-T.Y.: Conceptualization, supervision, project administration, methodology, resources, and writing—review and editing. J.H.K.: Investigation and data curation. J.Y.: Methodology, investigation, data curation and writing—review and editing. C.H.P.: formal analysis and data curation. J.-K.H.: Investigation, validation, writing—review and editing. N.G.S.R.: software and formal analysis. All authors have read and agreed to the published version of the manuscript.

**Funding:** This work was supported by the Technology Innovation Program (RS-2024-00436523) funded by the Ministry of Trade, Industry and Resources (MOTIR) and by the Fundamental Research Program (PNKA830) of the Korea Institute of Materials Science (KIMS), funded by the Ministry of Science and ICT (MSIT).

**Data Availability Statement:** The original contributions presented in this study are included in the article/Supplementary Material. Further inquiries can be directed to the corresponding authors.

**Conflicts of Interest:** The authors declare no conflicts of interest.

## References

1. Lin, J.; Ozan, S.; Li, Y.; Ping, D.; Tong, X.; Li, G.; Wen, C. Novel Ti-Ta-Hf-Zr alloys with promising mechanical properties for prospective stent applications. *Sci. Rep.* **2016**, *6*, 37901. [CrossRef]
2. Disegi, J.A.; Roach, M.D.; McMillan, R.D.; Shultzabarger, B.T. Alpha plus beta annealed and aged Ti-15 Mo alloy for high strength implant applications. *J. Biomed. Mater. Res. B Appl. Biomater.* **2017**, *105*, 2010–2018. [CrossRef]
3. Jin, H.; Wei, K.; Li, J.; Zhou, J.; Peng, W. Research development of titanium alloy in aerospace industry. *Chin. J. Nonferrous Met.* **2015**, *25*, 280–292.
4. Maurya, A.K.; Hwang, J.-W.; Yeom, J.-T.; Kim, J.H.; Yang, J.; Kim, J.H.; Lim, J.; Lee, S.W.; Park, C.H.; Hong, J.K.; et al. Optimized process design for uniform microstructure and high-strength Ti-6Al-4 V alloy fasteners in aerospace applications. *Met. Mater. Int.* **2025**, *32*, 1983–1995. [CrossRef]
5. Davis, A.E.; Kennedy, J.R.; Ding, J.; Prangnell, P.B. The effect of processing parameters on rapid-heating β recrystallization in inter-pass deformed Ti-6Al-4V wire-arc additive manufacturing. *Mater. Charact.* **2020**, *163*, 110298. [CrossRef]
6. Ho, A.; Zhao, H.; Fellowes, J.W.; Martina, F.; Davis, A.E.; Prangnell, P.B. On the origin of microstructural banding in Ti-6Al-4V wire-arc based high deposition rate additive manufacturing. *Acta Mater.* **2019**, *166*, 306–323. [CrossRef]
7. McAndrew, A.R.; Rosales, M.A.; Colegrove, P.A.; Hönnige, J.R.; Ho, A.; Fayolle, R.; Eyitayo, K.; Stan, I.; Sukrongpang, P.; Crochemore, A.; et al. Interpass rolling of Ti-6Al-4V wire + arc additively manufactured features for microstructural refinement. *Addit. Manuf.* **2018**, *21*, 340–349. [CrossRef]
8. Hu, M.; Dong, L.; Zhang, Z.; Lei, X.; Yang, R.; Sha, Y. Effects of multi-pass drawing strain and heat treatment on microstructure, texture and mechanical properties of Ti-6Al-4V alloy. *Mater. Sci. Eng. A* **2019**, *757*, 70–83. [CrossRef]
9. Jovanović, M.T.; Tadić, S.; Zec, S.; Mišković, Z.; Bobić, I. The effect of annealing temperatures and cooling rates on microstructure and mechanical properties of investment cast Ti-6Al-4V alloy. *Mater. Des.* **2006**, *27*, 192–199. [CrossRef]
10. Guo, L.; Fan, X.; Yu, G.; Yang, H. Microstructure control techniques in primary hot working of titanium alloy bars: A review. *Chin. J. Aeronaut.* **2016**, *29*, 30–40. [CrossRef]
11. Zhao, Q.; Yang, F.; Torrens, R.; Bolzoni, L. Comparison of hot deformation behaviour and microstructural evolution for Ti-5Al-5V-5Mo-3Cr alloys prepared by powder metallurgy and ingot metallurgy approaches. *Mater. Des.* **2019**, *169*, 107682. [CrossRef]
12. Roy, S.; Suwas, S. The influence of temperature and strain rate on the deformation response and microstructural evolution during hot compression of a titanium alloy Ti-6Al-4V-0.1B. *J. Alloys Compd.* **2013**, *548*, 110–125. [CrossRef]
13. Yoshino, M.; Shirakashi, T. Flow-stress equation including effects of strain-rate and temperature history. *Int. J. Mech. Sci.* **1997**, *39*, 1345–1362. [CrossRef]
14. Chaudhuri, A.; Behera, A.N.; Sarkar, A.; Kapoor, R.; Ray, R.K.; Suwas, S. Hot deformation behaviour of Mo-TZM and understanding the restoration processes involved. *Acta Mater.* **2019**, *164*, 153–164. [CrossRef]
15. Zhao, J.; Ding, H.; Zhao, W.; Huang, M.; Wei, D.; Jiang, Z. Modelling of the hot deformation behaviour of a titanium alloy using constitutive equations and artificial neural network. *Comput. Mater. Sci.* **2014**, *92*, 47–56. [CrossRef]

16. Honarmandi, P.; Aghaie-Khafri, M. Hot deformation behavior of Ti-6Al-4V alloy in β phase field and low strain rate. *Metallogr. Microstruct. Anal.* **2013**, *2*, 13–20. [CrossRef]
17. Lin, Y.C.; Zhao, C.-Y.; Chen, M.-S.; Chen, D.-D. A novel constitutive model for hot deformation behaviors of Ti-6Al-4V alloy based on probabilistic method. *Appl. Phys. A* **2016**, *122*, 716. [CrossRef]
18. Zhang, W.; Ding, H.; Zhao, J.; Yang, B.; Yang, W. Hot deformation behavior and processing maps of Ti-6Al-4V alloy with starting fully lamellar structure. *J. Mater. Res.* **2018**, *33*, 3677–3688. [CrossRef]
19. Karlik, B.; Olgac, A.V. Performance analysis of various activation functions in generalized MLP architectures of neural networks. *Int. J. Artif. Intell. Expert Syst.* **2011**, *1*, 111–122.
20. Moayed, F.A.; Shell, R.L. Application of artificial neural network models in occupational safety and health utilizing ordinal variables. *Ann. Occup. Hyg.* **2010**, *55*, 132–142. [CrossRef]
21. Reddy, N.S.; Lee, Y.H.; Park, C.H.; Lee, C.S. Prediction of flow stress in Ti-6Al-4V alloy with an equiaxed α+β microstructure by artificial neural networks. *Mater. Sci. Eng. A* **2008**, *492*, 276–282. [CrossRef]
22. Reddy, N.S.; Krishnaiah, J.; Hong, S.-G.; Lee, J.S. Modeling medium carbon steels by using artificial neural networks. *Mater. Sci. Eng. A* **2009**, *508*, 93–105. [CrossRef]
23. Ma, X.; Zeng, W.; Xu, B.; Sun, Y.; Xue, C.; Han, Y. Characterization of the hot deformation behavior of a Ti-22Al-25Nb alloy using processing maps based on the Murty criterion. *Intermetallics* **2012**, *20*, 1–7. [CrossRef]
24. Zhou, H.T.; Peng, Q.Z.; Yang, H.X.; Zhou, X.; Liu, R.R.; Peng, Y.; Zhong, F.H. Dynamic recrystallization during hot deformation of GH690 alloy: A study using processing maps. *J. Nucl. Mater.* **2014**, *448*, 153–162. [CrossRef]
25. Seshacharyulu, T.; Medeiros, S.C.; Morgan, J.T.; Malas, J.C.; Frazier, W.G.; Prasad, Y.V.R.K. Hot deformation and microstructural damage mechanisms in extra-low interstitial (ELI) grade Ti-6Al-4V. *Mater. Sci. Eng. A* **2000**, *279*, 289–299. [CrossRef]
26. Narayana, P.L.; Li, C.-L.; Hong, J.-K.; Choi, S.-W.; Park, C.H.; Kim, S.-W.; Kim, S.E.; Reddy, N.S.; Yeom, J.-T. Characterization of hot deformation behavior and processing maps of Ti-19Al-22Mo alloy. *Met. Mater. Int.* **2019**, *25*, 1063–1071. [CrossRef]
27. Prasad, Y.V.R.K.; Gegel, H.L.; Doraivelu, S.M.; Malas, J.C.; Morgan, J.T.; Lark, K.A.; Barker, D.R. Modeling of dynamic material behavior in hot deformation: Forging of Ti-6242. *Metall. Trans. A* **1984**, *15*, 1883–1892. [CrossRef]
28. Liu, Q.; Hui, S.; Tong, K.; Yu, Y.; Ye, W.; Song, S.-Y. Investigation of high temperature behavior and processing map of Ti-6Al-4V-0.11Ru titanium alloy. *J. Alloys Compd.* **2019**, *787*, 527–536. [CrossRef]
29. Sakai, T.; Belyakov, A.; Kaibyshev, R.; Miura, H.; Jonas, J.J. Dynamic and post-dynamic recrystallization under hot, cold and severe plastic deformation conditions. *Prog. Mater. Sci.* **2014**, *60*, 130–207. [CrossRef]
30. Quan, G.-Z.; Wen, H.-R.; Pu, S.-A.; Zou, Z.-Y.; Wu, D.-S. Identification of stable processing parameters in Ti-6Al-4V alloy from a wide temperature range across β transus and a large strain rate range. *High Temp. Mater. Process.* **2015**, *34*, 715–729. [CrossRef]
31. Poletti, C.; Germain, L.; Warchomicka, F.; Dikovits, M.; Mitsche, S. Unified description of the softening behavior of beta-metastable and alpha+beta titanium alloys during hot deformation. *Mater. Sci. Eng. A* **2016**, *651*, 280–290. [CrossRef]
32. Mandal, S.; Bhaduri, A.K.; Sarma, V.S. A study on microstructural evolution and dynamic recrystallization during isothermal deformation of a Ti-modified austenitic stainless steel. *Metall. Mater. Trans. A* **2011**, *42*, 1062–1072. [CrossRef]
33. Maurya, A.K.; Yeom, J.-T.; Kang, S.W.; Park, C.H.; Hong, J.-K.; Reddy, N.S. Optimization of hybrid manufacturing process combining forging and wire-arc additive manufactured Ti-6Al-4V through hot deformation characterization. *J. Alloys Compd.* **2022**, *894*, 162453. [CrossRef]
34. Semiatin, S.L.; Seetharaman, V.; Weiss, I. The thermomechanical processing of alpha/beta titanium alloys. *J. Miner. Met. Mater. Soc.* **1997**, *49*, 33–39. [CrossRef]
35. Behera, A.N.; Murty, T.N.; Sarkar, A.; Kapoor, R.; Singh, R.N.; Vaibhaw, K.; Arora, U.K.; Kapoor, K. Deformation behaviour and microstructure evolution of Ti-2.3Al-2.6Zr alloy in the temperature range of 700–1000 °C. *J. Alloys Compd.* **2024**, *1008*, 176791. [CrossRef]
36. *ASTM B600-11*; Standard Guide for Descaling and Cleaning Titanium and Titanium Alloy Surfaces. ASTM International: West Conshohocken, PA, USA, 2011.
37. Li, H.; Zhao, Z.; Guo, H.; Yao, Z.; Ning, Y.; Miao, X.; Ge, M. Effect of initial alpha lamellar thickness on deformation behavior of a near-α high-temperature alloy during thermomechanical processing. *Mater. Sci. Eng. A* **2017**, *682*, 345–353. [CrossRef]
38. Lütjering, G. Influence of processing on microstructure and mechanical properties of (α+β) titanium alloys. *Mater. Sci. Eng. A* **1998**, *243*, 32–45. [CrossRef]
39. Zhang, J.; Liu, H.; Zheng, J.; Ji, J.; Shi, Y.; Jia, L.; Yan, Z.; Dong, B.; Xue, Y. Microstructure characterization of hot isostatic pressed Ti-6Al-4V alloy under uniaxial compression and post heat treatment. *J. Mater. Res. Technol.* **2021**, *15*, 7070–7084. [CrossRef]

40. Singh, A.K.; Schwarzer, R.A. Texture and anisotropy of mechanical properties in titanium and its alloys. *Int. J. Mater. Res.* **2000**, *91*, 702–716. [CrossRef]
41. Hémery, S.; Villechaise, P.; Banerjee, D. Microplasticity at room temperature in $\alpha/\beta$ titanium alloys. *Metall. Mater. Trans. A* **2020**, *51*, 4931–4969. [CrossRef]

**Disclaimer/Publisher's Note:** The statements, opinions and data contained in all publications are solely those of the individual author(s) and contributor(s) and not of MDPI and/or the editor(s). MDPI and/or the editor(s) disclaim responsibility for any injury to people or property resulting from any ideas, methods, instructions or products referred to in the content.